





**First-principles Landau-like potential for BiFeO<sub>3</sub> and related materials**Natalya S. Fedorova <sup>1,\*</sup>, Dmitri E. Nikonov <sup>2</sup>, Hai Li <sup>2</sup>, Ian A. Young<sup>2</sup> and Jorge Íñiguez <sup>1,3,†</sup><sup>1</sup>*Materials Research and Technology Department, Luxembourg Institute of Science and Technology, 5 Avenue des Hauts-Fourneaux, L-4362 Esch/Alzette, Luxembourg*<sup>2</sup>*Components Research, Intel Corporation, Hillsboro, 97124 Oregon, USA*<sup>3</sup>*Department of Physics and Materials Science, University of Luxembourg, 41 Rue du Brill, L-4422 Belvaux, Luxembourg*

(Received 1 April 2022; revised 22 September 2022; accepted 26 September 2022; published 21 October 2022)

In this paper, we introduce the simplest, lowest-order Landau-like potential for BiFeO<sub>3</sub> and La-doped BiFeO<sub>3</sub> as an expansion around the paraelectric cubic phase in powers of polarization, FeO<sub>6</sub> octahedral rotations, and strains. We present an analytical approach for computing the model parameters from density-functional theory. We illustrate our approach by computing the potentials for BiFeO<sub>3</sub> and La<sub>0.25</sub>Bi<sub>0.75</sub>FeO<sub>3</sub> and show that, overall, we are able to capture the first-principles results accurately, including properties that were not considered for the calculation of the model parameters. The computed models allow us to identify and explain the main interactions controlling the relative stability of the competing low-energy phases of these compounds.

DOI: [10.1103/PhysRevB.106.165122](https://doi.org/10.1103/PhysRevB.106.165122)**I. INTRODUCTION**

Magnetoelectric multiferroics, materials that simultaneously show magnetic and electric orders, are of significant interest, since the coexistence and coupling of these orders hold great potential for development of multifunctional devices [1,2]. BiFeO<sub>3</sub> is among the most exciting and extensively studied representatives of this family because it displays both orders at room temperature [3].

Ferroelectricity appears in BiFeO<sub>3</sub> at  $T_C \sim 1100$  K [4,5]. Below  $T_C$ , it has a rhombohedrally distorted perovskite structure (space group  $R3c$ , No. 161) [6,7], which differs from the perfect cubic phase by the presence of two distortions: (i) polar displacements of Bi<sup>3+</sup> and Fe<sup>3+</sup> cations with respect to O<sup>2-</sup> anions (Bi<sup>3+</sup> dominates due to its stereochemically active 6s lone pairs [8]), giving rise to a spontaneous polarization  $\mathbf{P}$  of up to 100  $\mu\text{C}/\text{cm}^2$  along a pseudocubic  $\langle 111 \rangle$  direction [9,10] and (ii) antiphase rotations  $\mathbf{R}$  of the FeO<sub>6</sub> octahedra about the same pseudocubic  $\langle 111 \rangle$  direction as the polarization ( $a^-a^-a^-$  in Glazer's notation [11]) [12,13]. (In the following, all directions are in the pseudocubic setting.)

Below  $T_N \sim 640$  K, BiFeO<sub>3</sub> also shows G-type antiferromagnetic (G-AFM) order with the nearest-neighbor Fe spins antialigned [4,14]. The canting of the Fe spins driven by Dzyaloshinskii-Moriya (DM) interaction [15,16] can give rise to a weak magnetization in this material. The DM interaction relies on the symmetry breaking caused by the FeO<sub>6</sub> octahedral tilts of BiFeO<sub>3</sub> [12]; indeed, the phase of the octahedral rotations defines the sign of the DM vector and, in turn, that

of the weak magnetization. In bulk BiFeO<sub>3</sub>, an incommensurate cycloidal spiral is superimposed on the G-AFM order, yielding a zero net magnetization [17]. This cycloid, however, can be suppressed by doping in bulk systems [18] and by epitaxial constraints in BiFeO<sub>3</sub> films [19–22]. Therefore, ferroelectricity can coexist with weak ferromagnetism in BiFeO<sub>3</sub> at ambient conditions.

Additionally, a 180° deterministic switching of the DM vector and weak magnetization by an electric field has been reported from a combined experimental and theoretical study of BiFeO<sub>3</sub> films grown on DyScO<sub>3</sub> substrates [22]. It is proposed that the magnetoelectric switching is the result of a peculiar polarization reversal that is found to occur in two steps, a 109° rotation followed by a 71° rotation (or vice versa); further, the FeO<sub>6</sub> octahedral tilts are believed to reverse together with the polarization, resulting in the observed reversal of the weak magnetic moment. Note that octahedral tilts will typically not follow polarization in a single-step 180° reversal and, therefore, a two-step switching path is crucial for controlling the weak magnetization in BiFeO<sub>3</sub> by an electric field. These observations make BiFeO<sub>3</sub> a promising candidate for applications in magnetoelectric memory elements. However, to be technologically relevant, switching characteristics have to be optimized such that coercive voltages are below 100 mV and switching times fall in the range of 10–1000 ps [23,24]. Hence, the current challenge is to optimize the ferroelectric switching in BiFeO<sub>3</sub> while retaining the two-step path and magnetoelectric control.

One of the efficient strategies for optimizing polarization switching in BiFeO<sub>3</sub> is doping by La. Indeed, since polarization in this compound largely originates from the 6s lone pairs of the Bi<sup>3+</sup> cations, their substitution by isovalent, lone-pair-free cations leads to a reduction of the polar distortion [3,25,26]. For example, it has been experimentally demonstrated that 15–20% La-doped BiFeO<sub>3</sub> films show a polarization which is up to 60% smaller than that of pure BiFeO<sub>3</sub> films [24,27]. Further, first-principles calculations have

\*natalya.fedorova@list.lu

†jorge.iniguez@list.lu

predicted that substitution of Bi by La cations reduces the energy barrier between polar states by up to 50% for 25% doping. This, in turn, leads to a reduction of coercive voltages (down to 0.8 V for a 100 nm film), enabling low-power switching [24]. Additionally, a significant reduction of switching times has been demonstrated for  $\text{La}_{0.15}\text{Bi}_{0.75}\text{FeO}_3$  films compared to pure  $\text{BiFeO}_3$  in a wide range of applied electric fields [28]. Nevertheless, further improvement requires understanding the origin of the two-step polarization switching in  $\text{BiFeO}_3$  and related materials, as well as search for other strategies for manipulating the switching energy landscape. For that purpose, dynamical simulations of polarization switching based on phenomenological models of the free energy can be very helpful.

Landau free-energy potentials [29–32], together with the Landau-Khalatnikov time-evolution equation [33], offer a practical scheme to investigate switching in ferroelectrics. In this approach, one expands the energy of the compound around the reference paraelectric phase in powers of the relevant order parameters, keeping only terms compatible with the crystal symmetry [34]. It is important to note that the reliability of such simulations depends on the choice of the free energy expansion's coefficients, which can be obtained either by fitting to experimental data or from first-principles calculations [34]. In compounds as complex as  $\text{BiFeO}_3$ , which feature multiple primary order parameters, deriving a suitable Landau potential from experimental information is all but impossible; hence, there is a clear need for the development of first-principles approaches.

In this paper, we introduce the simplest, lowest-order Landau-like potential able to reproduce the energies and structures of the low-energy polymorphs of  $\text{BiFeO}_3$  and related materials. We present an analytical approach to compute the model parameters from density functional theory (DFT) and apply it to  $\text{BiFeO}_3$  and  $\text{La}_{0.25}\text{Bi}_{0.75}\text{FeO}_3$ . We demonstrate the overall accuracy of the obtained potentials and discuss an effective way to treat intermediate compositions. Finally, we discuss the physics captured by the model, namely, the interaction between polarization and  $\text{FeO}_6$  octahedral tilts, how it affects the energetics of different  $\text{BiFeO}_3$  polymorphs, as well as the effects of La doping.

## II. COMPUTATIONAL DETAILS

All calculations are performed using the DFT [35,36] implementation in the VIENNA AB INITIO SIMULATION PACKAGE (VASP) [37]. For the exchange-correlation potential, we use the generalized gradient approximation optimized for solids [38], with a Hubbard  $U$  correction (within Dudarev's scheme [39] and  $U = 4$  eV) for a better treatment of iron's  $3d$  electrons. We treat the interaction between core and valence electrons by the projector-augmented plane wave method [37,40], solving explicitly for 15 electrons of Bi ( $5d^{10}6s^26p^3$ ), 9 of La ( $5p^66s^25d^1$ ), 14 of Fe ( $3p^63d^74s^1$ ), and 6 of O ( $2s^22p^4$ ). We use a plane-wave basis set with a cutoff energy of 500 eV. We use a  $3 \times 3 \times 3$   $\Gamma$ -centered Monkhorst-Pack  $k$ -point grid for reciprocal space integrals in the Brillouin zone corresponding to a 40-atom cell that is a  $2 \times 2 \times 2$  multiple of the five-atom perovskite unit [see Fig. 1(a)]. We ensure that these choices provide a good level of convergence for

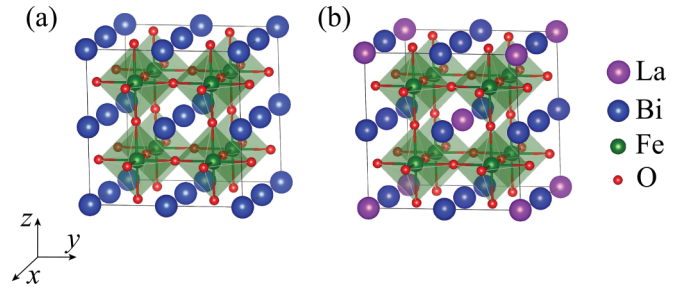


FIG. 1. Sketch of the 40-atom supercell used in our simulations of (a)  $\text{BiFeO}_3$  and (b)  $\text{La}_{0.25}\text{Bi}_{0.75}\text{FeO}_3$ .

the quantities of interest. All simulations are performed with the G-type antiferromagnetic order of Fe magnetic moments imposed. This order has the lowest energy for all considered  $\text{BiFeO}_3$  polymorphs except the tetragonal P[001] and P[001]+R[001] (the notations for the polymorphs are introduced in Sec. III B 1), for which the C-type antiferromagnetic order (nearest-neighboring Fe spins coupled antiferromagnetically within  $ab$  planes, and ferromagnetically between adjacent  $ab$  planes) is more favorable. Since magnetism is not explicitly treated in our effective potential, and since the tetragonal polymorphs are the least relevant for our purposes of studying polarization switching in  $\text{BiFeO}_3$  and related materials, we impose the G-AFM order in all our calculations.

In the lattice optimizations, the structures are considered to be relaxed when the forces acting on the atoms are below 0.01 eV/Å. We calculate elastic constants by finite differences using the strain-stress relationship [41].

## III. FORMALISM

### A. Landau-like potential

In this section, we introduce the potential for  $\text{BiFeO}_3$  and La-doped  $\text{BiFeO}_3$  as an expansion around the reference paraelectric cubic phase in powers of the following order parameters: (i) the three-dimensional electric polarization  $\mathbf{P} = (P_x, P_y, P_z)$ , (ii) the antiphase rotations of  $\text{FeO}_6$  octahedra  $\mathbf{R} = (R_x, R_y, R_z)$ , and (iii) the strain  $\boldsymbol{\eta} = (\eta_{xx}, \eta_{yy}, \eta_{zz}, \eta_{yz}, \eta_{xz}, \eta_{xy})$ , where  $\eta_{xx} = \epsilon_{xx}$ ,  $\eta_{yy} = \epsilon_{yy}$ ,  $\eta_{zz} = \epsilon_{zz}$ ,  $\eta_{yz} = 2\epsilon_{yz}$ ,  $\eta_{xz} = 2\epsilon_{xz}$ , and  $\eta_{xy} = 2\epsilon_{xy}$ , and  $\epsilon_{ij}$  are the components of the symmetric part of the homogeneous strain tensor. The resulting expression for the potential (per perovskite unit cell) is written as follows:

$$F(\mathbf{P}, \mathbf{R}, \boldsymbol{\eta}) = F_0 + F(\mathbf{P}) + F(\mathbf{R}) + F(\boldsymbol{\eta}) + F(\mathbf{P}, \mathbf{R}) + F(\mathbf{P}, \boldsymbol{\eta}) + F(\mathbf{R}, \boldsymbol{\eta}). \quad (1)$$

Here,  $F_0$  is the energy of the reference cubic phase.  $F(\mathbf{P})$ ,  $F(\mathbf{R})$ , and  $F(\boldsymbol{\eta})$  are the energy contributions solely due to polarization,  $\text{FeO}_6$  octahedral rotations and strain, respectively, which we write as follows:

$$F(\mathbf{P}) = A_P(P_x^2 + P_y^2 + P_z^2) + B_P(P_x^2 + P_y^2 + P_z^2)^2 + C_P(P_x^2 P_y^2 + P_y^2 P_z^2 + P_z^2 P_x^2), \quad (2)$$

$$F(\mathbf{R}) = A_R(R_x^2 + R_y^2 + R_z^2) + B_R(R_x^2 + R_y^2 + R_z^2)^2 + C_R(R_x^2 R_y^2 + R_y^2 R_z^2 + R_z^2 R_x^2), \quad (3)$$

$$F(\boldsymbol{\eta}) = \frac{1}{2}C_{11}(\eta_{xx}^2 + \eta_{yy}^2 + \eta_{zz}^2) + C_{12}(\eta_{xx}\eta_{yy} + \eta_{yy}\eta_{zz} + \eta_{zz}\eta_{xx}) + \frac{1}{2}C_{44}(\eta_{yz}^2 + \eta_{xz}^2 + \eta_{xy}^2). \quad (4)$$

We truncate the expansion in  $\mathbf{P}$  and  $\mathbf{R}$  at the fourth order, which is the minimum required to model structural instabilities. In turn, we only consider harmonic terms for the strains.

Then,  $F(\mathbf{P}, \mathbf{R})$ ,  $F(\mathbf{P}, \boldsymbol{\eta})$ , and  $F(\mathbf{R}, \boldsymbol{\eta})$  are the coupling terms, which we write as

$$F(\mathbf{P}, \mathbf{R}) = B_{PR}(P_x^2 + P_y^2 + P_z^2)(R_x^2 + R_y^2 + R_z^2) + C_{PR}(P_x^2 R_x^2 + P_y^2 R_y^2 + P_z^2 R_z^2) + C'_{PR}(P_x P_y R_x R_y + P_y P_z R_y R_z + P_z P_x R_z R_x), \quad (5)$$

$$F(\mathbf{P}, \boldsymbol{\eta}) = \gamma_{P111}(\eta_{xx}P_x^2 + \eta_{yy}P_y^2 + \eta_{zz}P_z^2) + \gamma_{P122}(\eta_{xx}(P_y^2 + P_z^2) + \eta_{yy}(P_z^2 + P_x^2) + \eta_{zz}(P_x^2 + P_y^2)) + \gamma_{P423}(\eta_{yz}P_y P_z + \eta_{xz}P_z P_x + \eta_{xy}P_x P_y), \quad (6)$$

$$F(\mathbf{R}, \boldsymbol{\eta}) = \gamma_{R111}(\eta_{xx}R_x^2 + \eta_{yy}R_y^2 + \eta_{zz}R_z^2) + \gamma_{R122}(\eta_{xx}(R_y^2 + R_z^2) + \eta_{yy}(R_z^2 + R_x^2) + \eta_{zz}(R_x^2 + R_y^2)) + \gamma_{R423}(\eta_{yz}R_y R_z + \eta_{xz}R_z R_x + \eta_{xy}R_x R_y). \quad (7)$$

Here we restrict ourselves to the lowest-order symmetry-allowed couplings between the considered order parameters. Note that, in these equations,  $A$ ,  $B$ ,  $C$ ,  $C'$ , and  $\gamma$  are the material-dependent expansion coefficients that we compute using DFT as detailed in Sec. III B. The coefficients  $C_{11}$ ,  $C_{12}$ , and  $C_{44}$  in Eq. (4), as well as  $\gamma$  parameters in Eqs. (5)–(7), are given in Voigt notation for compactness.

## B. Computing the potential parameters

We now describe the approach to compute the expansion coefficients of the Landau-like potential introduced in Sec. III A. We mainly focus on an analytical approach, but also discuss briefly a numerical scheme for comparison.

### 1. Data set

We first identify the states or polymorphs that we want our models to describe. We consider the ground state as well as the low-energy polymorphs of the material, including the states that might be relevant for polarization switching. We thus define a data set of first-principles results corresponding to the energies and structures of such polymorphs.

Before we continue, let us introduce a convenient notation for the polymorphs we consider: We write P(R)[...]*c* or P[...]+R[...]*c*, where the first letter, P or R, indicates whether the structure presents a polar distortion or FeO<sub>6</sub> octahedral tilts, respectively (if both distortions appear, we indicate it by P+R); then [001] or [111] shows the axis along/about which the corresponding distortion is oriented; finally, *c* indicates that the cubic cell is kept fixed. Thus, for example, the polymorph P[001]*c* is characterized by a polar distortion along the [001] direction and its cell is fixed to that of cubic reference

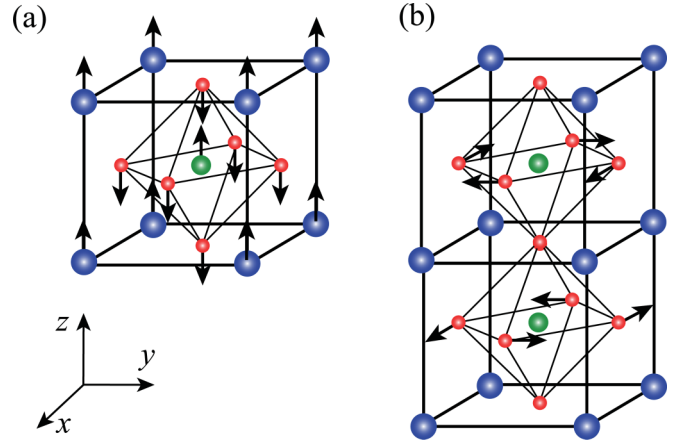


FIG. 2. Ionic displacement patterns corresponding to (a) a polar distortion mode along the [001] pseudocubic direction and (b) FeO<sub>6</sub> octahedral rotations about the same axis. Arrows indicate the directions of the ionic displacements and do not reflect their relative amplitudes. Blue, green, and red circles indicate Bi, Fe, and O ions, respectively.

structure. For simplicity, we also introduce short notations for all the polymorphs of interest, such as 1c for the state P[001]*c*. We summarize all the notations for the polymorphs and the corresponding order parameters in Table I.

**BiFeO<sub>3</sub>.** The starting point for constructing the data set is the already-mentioned 40-atom supercell compatible with the G-type antiferromagnetic order and the antiphase rotations of the FeO<sub>6</sub> octahedra. First, we run a DFT simulation to optimize the volume of the cubic phase of BiFeO<sub>3</sub> using this supercell. Next, we use the optimized structure to construct six polymorphs (1c to 6c in Table I) by imposing the polar distortion and/or antiphase octahedral rotation along/about either the [001] or [111] directions while keeping the volume and shape of the supercell fixed (the corresponding ionic displacement patterns are illustrated in Fig. 2). We use DFT to optimize the ionic positions in these polymorphs and calculate the energies  $E_s$  of the resulting structures, where the index  $s$  labels polymorphs in the data set. Additionally, we also consider the state we call P[111̄]+R[111]*c* (7c); here, we impose a polar distortion and octahedral tilts with amplitudes typical of BiFeO<sub>3</sub>, but oblique to each other. This structure does not correspond to a special point of the energy landscape; therefore, we do not perform a structural optimization and only compute its energy, which is needed to obtain the coefficient  $C'_{PR}$ , as we will show in Sec. III B 2.

Next, we consider the first six polymorphs mentioned above, but now allowing for changes in the shape and volume of the supercell (structures 1–6 in Table I; note we omit *c* in the notation).

In all cases, we extract the displacements  $\mathbf{u}_{Bi,s}$  ( $u_{Bi,s}$  are in angstrom) of the Bi cations with respect to the corresponding O anion cages. We average the values of these displacements over all Bi ions to obtain  $\bar{\mathbf{u}}_{Bi,s}$ . Since the Bi off-centering largely determines the electric polarization in BiFeO<sub>3</sub>, we estimate  $\mathbf{P}_s$  for the considered polymorphs as  $\mathbf{P}_s = K_0 \bar{\mathbf{u}}_{Bi,s}$ , where  $K_0 = P_0/\bar{u}_{Bi,6}$ ,  $P_0 = 0.58$  C/m<sup>2</sup>, and  $\bar{\mathbf{u}}_{Bi,6}$  is the average Bi off-centering in the ground state P[111̄]+R[111]. This

TABLE I. Polymorphs (labeled by  $s$ ) included in the data set for computing the potential's coefficients and the notations for their polarizations  $\mathbf{P}_s$ , FeO<sub>6</sub> octahedral rotations  $\mathbf{R}_s$ , and components of the strain tensor  $\eta_s$ .

Polymorph		$\mathbf{P}$	$\mathbf{R}$	$\eta$
1c	P[001]c	(0,0, $P_{1c}$ )	(0,0,0)	(0,0,0,0,0,0)
2c	P[111]c	( $P_{2c}, P_{2c}, P_{2c}$ )	(0,0,0)	(0,0,0,0,0,0)
3c	R[001]c	(0,0,0)	(0,0, $R_{3c}$ )	(0,0,0,0,0,0)
4c	R[111]c	(0,0,0)	( $R_{4c}, R_{4c}, R_{4c}$ )	(0,0,0,0,0,0)
5c	P[001]+R[001]c	(0,0, $P_{5c}$ )	(0,0, $R_{5c}$ )	(0,0,0,0,0,0)
6c	P[111]+R[111]c	( $P_{6c}, P_{6c}, P_{6c}$ )	( $R_{6c}, R_{6c}, R_{6c}$ )	(0,0,0,0,0,0)
7c	P[11 $\bar{1}$ ]+R[111]c	( $P_{7c,\perp}, P_{7c,\perp}, P_{7c,\parallel}$ )	( $R_{7c,\perp}, R_{7c,\perp}, R_{7c,\parallel}$ )	(0,0,0,0,0,0)
1	P[001]	(0,0, $P_1$ )	(0,0,0)	( $\eta_{1,\perp}, \eta_{1,\perp}, \eta_{1,\parallel}, 0, 0, 0$ )
2	P[111]	( $P_2, P_2, P_2$ )	(0,0,0)	( $\eta_2, \eta_2, \eta_2, s_2, s_2, s_2$ )
3	R[001]	(0,0,0)	( $R_3, 0, 0$ )	( $\eta_{3,\parallel}, \eta_{3,\perp}, \eta_{3,\perp}, 0, 0, 0$ )
4	R[111]	(0,0,0)	( $R_4, R_4, R_4$ )	( $\eta_4, \eta_4, \eta_4, s_4, s_4, s_4$ )
5	P[001]+R[001]	(0,0, $P_5$ )	(0,0, $R_5$ )	( $\eta_{5,\perp}, \eta_{5,\perp}, \eta_{5,\parallel}, 0, 0, 0$ )
6	P[111]+R[111]	( $P_6, P_6, P_6$ )	( $R_6, R_6, R_6$ )	( $\eta_6, \eta_6, \eta_6, s_6, s_6, s_6$ )

choice of  $P_0$  ensures that the spontaneous polarization of the P[111]+R[111] polymorph is  $\mathbf{P}_6 = P_0(1, 1, 1)$  which gives the magnitude of  $\mathbf{P}_6$  around its experimentally determined value of 1 C/m<sup>2</sup>.

Similarly, we compute the rotation angles of the FeO<sub>6</sub> octahedra  $\mathbf{R}_s$  about the pseudocubic axes, from which we obtain the amplitude of the antiphase tilt pattern,  $\bar{\mathbf{R}}_s$ . Finally, in the cases where the shape and volume of the cell are allowed to relax, we also extract the components of the strain tensor  $\eta_s$ . The obtained results constitute our data set, which is presented in Table S1 of the Supplemental Material [42].

*La-doped* BiFeO<sub>3</sub>. Experimentally, La dopants distribute quasirandomly in the BiFeO<sub>3</sub> lattice, so the macroscopic symmetry (cubic for the paraelectric phase, rhombohedral for the ground state) is only recovered when a sufficiently large sample volume is considered. Unfortunately, reproducing such a situation in a DFT calculation has a prohibitive computational cost; thus, here we assume that a particular highly ordered La arrangement, where the dopants are as separated as possible from one another *and* which respects the cubic symmetry of the reference lattice, is a good approximation to the average experimental configuration. This approach allows us to derive Landau potentials for doped materials, with the experimentally relevant symmetry properties, from relatively inexpensive DFT calculations. Admittedly, a careful (computationally costly) validation of its accuracy remains for future work.

For a 25% La doping, the symmetric arrangement we use is shown in Fig. 1(b). In this arrangement, the dopants are placed at third-nearest-neighbor (3NN) A sites. In principle, for this concentration of La, there are two other possibilities to place La dopants within the 40-atom supercell: (i) at first-nearest-neighbor A sites and (ii) at second-nearest-neighbor (2NN) A sites. In fact, our calculations show that the 2NN arrangement is more favorable than the 3NN by about 1 meV per five-atom cell in cubic and P[111]+R[111] polymorphs with fully relaxed cells. These small energy differences between the considered La orderings are consistent with the experimental observation of randomly distributed La dopants. Note, however, that 2NN arrangement leads to a symmetry reduction of both cubic and P[111]+R[111] phases

that is not observed experimentally (for example, it would yield a monoclinic ground state instead of rhombohedral). Hence, since the tendency of the La atoms to order is very weak, and since experimental evidence suggests that our Landau potential should describe reference cubic and ferroelectric rhombohedral phases, working with the 3NN arrangement shown in Fig. 1(b) seems the best practical approximation to treat La<sub>x</sub>Bi<sub>1-x</sub>FeO<sub>3</sub> with  $x = 0.25$ .

Additionally, it is worth noting that, instead of considering the dopants explicitly, methods like the virtual crystal approximation (VCA) [43] can be an alternative in some cases. Within the VCA, doping is taken into account by considering virtual atoms that are described by a pseudopotential constructed as a weighted average of the pseudopotentials of the corresponding real atoms [44] (La and Bi in our case). The advantage of the VCA is that it allows to study any doping concentration with no need to construct large supercells and preserving the high symmetry of the reference lattice. However, the VCA is not general, and should be avoided in the cases when the real atoms have significantly different valence electronic structures. For example, a mixture of Fe<sup>3+</sup> (with a 3d<sup>5</sup> valence configuration) and Ti<sup>4+</sup> (with a 3d<sup>0</sup> valence configuration) is not treatable within the VCA.

Having chosen a suitable, symmetric dopant arrangement, we optimize the cubic cell of the reference paraelectric structure using DFT. Next, we use this structure to construct the sets of polymorphs 1c to 7c and 1 to 6, in analogy to the case of pure BiFeO<sub>3</sub>. For the case of a 25% La composition, the obtained  $\mathbf{P}_s$ ,  $\mathbf{R}_s$ ,  $\eta_s$ , and  $E_s$  of their optimized structures are summarized in Table S2 of the Supplemental Material [42].

Note that we encountered difficulties in constructing the data set for La<sub>1-x</sub>Bi<sub>x</sub>FeO<sub>3</sub> compositions with an intermediate content of La ( $0 < x < 0.25$ ). For example, for La<sub>0.125</sub>Bi<sub>0.875</sub>FeO<sub>3</sub>, one can easily construct a paraelectric reference by substituting a single Bi atom in the supercell of Fig. 1(a). However, we observed that the P[001]+R[001]c and P[001]+R[001] polymorphs relax to the lower symmetry phases displaying additional (and large) in-phase rotations of the FeO<sub>6</sub> octahedra. These extra distortions are secondary modes activated by the symmetry breaking associated to the combination of polar and antiphase orders together with the



considered arrangement of La dopants. These distortions are not expected to occur experimentally, as the La dopants are largely disordered in real samples, and such in-phase tilts may occur locally at most. Moreover, they cannot be treated within our simple potentials (an explicit consideration of in-phase tilts would be required) and complicate the definition of the data set. Hence, here we do not compute models for such intermediate compositions. Nevertheless, as we show in Sec. IV C, suitable potentials can be obtained by interpolation between those obtained for neighboring (well-behaved) compositions.

## 2. Analytical approach

The approach introduced in this section allows full control of the information used to compute the parameters of the potential. To achieve that, we derive an analytical expression for each of the potential coefficients, in terms of  $E_s$ ,  $\mathbf{P}_s$ ,  $\mathbf{R}_s$ , and  $\boldsymbol{\eta}_s$  of the polymorphs in the data set (see Sec. III B 1). To obtain such formulas, we write the expressions for the energies of the polymorphs using Eqs. (1)–(7) and impose the zero-derivative condition  $\partial F/\partial\phi_{i,s} = 0$ , where  $\phi_{i,s}$  is the  $i$ th component of order parameter  $\phi$  evaluated for polymorph  $s$ . These zero-derivative conditions are crucial to ensure that the computed model will faithfully describe the physics of BiFeO<sub>3</sub>, namely, we find that, if they are excluded from the fit, one typically obtains models that are unbounded from below.

Let us illustrate our procedure by presenting in detail the case of the parameters  $A_P$ ,  $B_P$ , and  $C_P$  of Eq. (2). We consider two polar-only polymorphs with fixed cubic cell, P[001]c (1c) and P[111]c (2c), and use the notation for their polarization components introduced in Table I,  $\mathbf{P}_{1c} = (0, 0, P_{1c})$  and  $\mathbf{P}_{2c} = (P_{2c}, P_{2c}, P_{2c})$ . Then, from Eq. (2) we can write the polymorph energies

$$E_{1c} = A_P P_{1c}^2 + B_P P_{1c}^4 \quad (8)$$

and

$$E_{2c} = 3A_P P_{2c}^2 + 3(3B_P + C_P)P_{2c}^4. \quad (9)$$

By taking the derivatives of these energies with respect to  $P_{1c}$  and  $P_{2c}$ , and setting them equal to zero, we obtain the following equations for the equilibrium values of  $P_{1c}$  and  $P_{2c}$ :

$$P_{1c}^2 = -\frac{A_P}{2B_P} \quad (10)$$

and

$$P_{2c}^2 = -\frac{A_P}{2(3B_P + C_P)}. \quad (11)$$

Then, by using these expressions in Eqs. (8) and (9), we obtain, respectively,  $E_{1c}$  and  $E_{2c}$  as functions of the parameters of the potential, such as

$$E_{1c} = -\frac{A_P^2}{4B_P} \quad (12)$$

and

$$E_{2c} = -\frac{3A_P^2}{4(3B_P + C_P)}. \quad (13)$$

From Eq. (11), one can see that  $3B_P + C_P = -A_P/2P_{2c}^2$ . By using this in Eq. (13), one can straightforwardly obtain the

TABLE II. Conditions used to derive the analytical expressions for the potential's coefficients.  $E_s|\phi_{s,\text{eq}}$  denotes the energy of the polymorph  $s$  corresponding to the equilibrium value of order parameter  $\phi_s$ .  $\lambda = 1 \text{ m}^4 \text{ deg}^2/\text{C}^2$  is an *ad hoc* coefficient used to balance the units for the terms in  $f_{5c}$  and  $f_{6c}$  (see text).

Conditions	
$A_P$ $B_P$ $C_P$	$\frac{\partial E_{1c}}{\partial P_{1c}} = 0$ ; $\frac{\partial E_{2c}}{\partial P_{2c}} = 0$ ; $E_{1c} _{P_{1c,\text{eq}}}$ ; $E_{2c} _{P_{2c,\text{eq}}}$
$A_R$ $B_R$ $C_R$	$\frac{\partial E_{3c}}{\partial R_{3c}} = 0$ ; $\frac{\partial E_{4c}}{\partial R_{4c}} = 0$ ; $E_{3c} _{R_{3c,\text{eq}}}$ ; $E_{4c} _{R_{4c,\text{eq}}}$
$B_{PR}$ $C_{PR}$ $C'_{PR}$	$\frac{\partial E_{5c}}{\partial P_{5c}} + \lambda \frac{\partial E_{5c}}{\partial R_{5c}} = 0$ ; $\frac{\partial E_{6c}}{\partial P_{6c}} + \lambda \frac{\partial E_{6c}}{\partial R_{6c}} = 0$ ; $E_{7c}$
$\gamma_{P111}$	$\frac{\partial E_6}{\partial \eta_6} = 0$
$\gamma_{P122}$	$\frac{\partial E_1}{\partial \eta_{1,\perp}} = 0$ ; $\frac{\partial E_2}{\partial \eta_2} = 0$
$\gamma_{P423}$	$\frac{\partial E_6}{\partial s_6} = 0$
$\gamma_{R111}$	$\frac{\partial E_3}{\partial \eta_{3,\perp}} = 0$
$\gamma_{R122}$	$\frac{\partial E_3}{\partial \eta_{3,\perp}} = 0$ ; $\frac{\partial E_4}{\partial \eta_4} = 0$
$\gamma_{R423}$	$\frac{\partial E_4}{\partial s_4} = 0$

analytical expression for  $A_P$ :

$$A_P = \frac{2E_{2c}}{3P_{2c}^2}. \quad (14)$$

From Eq. (12), in turn, one can obtain

$$B_P = -\frac{A_P^2}{4E_{1c}}. \quad (15)$$

Finally, by combining Eqs. (13)–(15), we get:

$$C_P = \frac{3A_P^2}{4} \left( \frac{1}{E_{1c}} - \frac{1}{E_{2c}} \right). \quad (16)$$

Since  $E_{1c}$ ,  $E_{2c}$ , and  $P_{2c}$  are known from our first-principles calculations described above, the coefficients  $A_P$ ,  $B_P$ , and  $C_P$  can be directly computed using Eqs. (14)–(16), respectively.

Similarly, we can derive the analytical expressions for the remaining coefficients of our potential. The specific conditions and properties used in the derivation are summarized in Table II, and the resulting expressions are

$$A_R = \frac{2E_{4c}}{3R_{4c}^2}, \quad (17)$$

$$B_R = \frac{-A_R^2}{4E_{3c}}, \quad (18)$$

$$C_R = \frac{3A_R^2}{4} \left( \frac{1}{E_{3c}} - \frac{1}{E_{4c}} \right), \quad (19)$$

$$B_{PR} = \frac{f_{7c} - f_{5c}(C_{7c} - C'_{7c}) - \frac{1}{3}C'_{7c}f_{6c}}{B_{7c} - C_{7c} - 2C'_{7c}}, \quad (20)$$

where

$$B_{7c} = (2P_{7c,\perp}^2 + P_{7c,\parallel}^2)(2R_{7c,\perp}^2 + R_{7c,\parallel}^2), \quad (21)$$

$$C_{7c} = 2P_{7c,\perp}^2 R_{7c,\perp}^2 + P_{7c,\parallel}^2 R_{7c,\parallel}^2, \quad (22)$$

$$C'_{7c} = P_{7c,\perp}^2 R_{7c,\perp}^2 + 2P_{7c,\perp} P_{7c,\parallel} R_{7c,\perp} R_{7c,\parallel}, \quad (23)$$

$$f_{5c} = -\frac{A_P + \lambda A_R + 2B_P P_{5c}^2 + 2\lambda B_R R_{5c}^2}{\lambda P_{5c}^2 + R_{5c}^2} \quad (24)$$

and

$$f_{6c} = -\frac{1}{\lambda P_{6c}^2 + R_{6c}^2} (3A_P + 3\lambda A_R + 6(3B_P + C_P)P_{6c}^2 + 6\lambda(3B_R + C_R)R_{6c}^2), \quad (25)$$

where  $\lambda = 1 \text{ m}^4 \text{ deg}^2 / \text{C}^2$  is an *ad hoc* coefficient that allows us to combine two zero-derivative conditions (for polarization and tilts, respectively) into only one. Further, we have

$$f_{7c} = E_{7c} - (A_P(2P_{7c,\perp}^2 + P_{7c,\parallel}^2) + B_P(2P_{7c,\perp}^2 + P_{7c,\parallel}^2)^2 + C_P(P_{7c,\perp}^4 + 2P_{7c,\perp}^2 P_{7c,\parallel}^2) + A_R(2R_{7c,\perp}^2 + R_{7c,\parallel}^2) + B_R(2R_{7c,\perp}^2 + R_{7c,\parallel}^2)^2 + C_R(R_{7c,\perp}^4 + 2R_{7c,\perp}^2 R_{7c,\parallel}^2)), \quad (26)$$

$$C_{PR} = f_{5c} - B_{PR}, \quad (27)$$

$$C'_{PR} = \frac{1}{C'_{7c}} (f_{7c} - B_{7c} B_{PR} - C_{7c} C_{PR}), \quad (28)$$

$$\gamma_{P122} = \frac{(C_{12} - C_{11})\eta_{1,\perp}}{P_1^2} - \frac{C_{12}\eta_2}{P_2^2}, \quad (29)$$

$$\gamma_{P111} = -2\gamma_{P122} - \left( \eta_6 + \frac{(\gamma_{R111} + 2\gamma_{R122})R_6^2}{C_{11} + 2C_{12}} \right) \frac{C_{11} + 2C_{12}}{P_6^2}, \quad (30)$$

$$\gamma_{P423} = -\left( s_6 + \frac{\gamma_{R423}R_6^2}{C_{44}} \right) \frac{C_{44}}{P_6^2}, \quad (31)$$

$$\gamma_{R111} = \frac{2(C_{11} - C_{12})\eta_{3,\perp}}{R_3^2} - \frac{C_{11}\eta_4}{R_4^2}, \quad (32)$$

$$\gamma_{R122} = \frac{(C_{12} - C_{11})\eta_{3,\perp}}{R_3^2} - \frac{C_{12}\eta_4}{R_4^2}, \quad (33)$$

and

$$\gamma_{R423} = -\frac{C_{44}s_4}{R_4^2}. \quad (34)$$

Note that it is possible to choose other conditions, different from those described above and presented in Table II, to derive the expressions for the model parameters. For example, the coefficients  $A_P$ ,  $B_P$ , and  $C_P$  can be obtained as functions of  $P_{1c}$ ,  $P_{2c}$ , and  $E_{2c}$  instead of  $P_{2c}$ ,  $E_{1c}$ , and  $E_{2c}$  [as represented above by Eqs. (14)–(16), respectively]. Moreover, one can even consider other polymorphs, not included in the data set introduced in Sec. III B 1. For instance, the polarization and energy of the P[011]c polymorph can be used instead of P[001]c or P[111]c in the derivation of  $A_P$ ,  $B_P$ , and  $C_P$  coefficients. The potentials derived using these new expressions provide a description nearly as accurate as the initial parameter set; more details can be found in Sec. SII of the Supplemental Material [42]. Similarly, a parameter like  $\gamma_{P111}$  might be obtained from the

energies and structures of polar-only polymorphs, in analogy to what we do for  $\gamma_{R111}$  using tilt-only polymorphs. However, we find that this choice yields shear strains with incorrect sign for the P[111]+R[111] ground state of BiFeO<sub>3</sub>. By contrast, the condition we use to compute  $\gamma_{P111}$  (i.e.,  $\partial E_6 / \partial \eta_6 = 0$ ) includes the information about the ground state and corrects this problem. These difficulties reflect the simplicity of our low-order polynomial model, which can account (exactly) for only a small number of properties.

Finally, the elastic constants  $C_{11}$ ,  $C_{12}$ , and  $C_{44}$  are calculated directly from DFT.

### 3. Numerical approach

The numerical approach that we introduce in this section allows us to compute the potential coefficients using the information from all considered structural polymorphs. We focus here on the case of pure BiFeO<sub>3</sub>, noting that exactly the same procedure can be applied to La<sub>0.25</sub>Bi<sub>0.75</sub>FeO<sub>3</sub>.

We work with the BiFeO<sub>3</sub> polymorphs from the data set introduced in Sec. III B 1, namely, 1c to 7c and 1 to 6 of Table I. Based on the energies ( $E_s$ ) and structural parameters ( $\mathbf{P}_s$ ,  $\mathbf{R}_s$ , and  $\eta_s$ ) obtained from DFT, we construct an overdetermined system of linear equations, with the potential parameters as unknowns, using the expressions for the energy and zero derivatives corresponding to all polymorphs. (For the 7c state, the zero-derivative condition does not apply. Also, we use the elastic constants  $C_{11}$ ,  $C_{12}$ , and  $C_{44}$  directly obtained from DFT.) We solve this system of equations using the least squares method.

We find that the potential obtained using this approach provides less accurate predictions for the properties of the low-energy polymorphs of BiFeO<sub>3</sub> as compared to the analytical approach introduced in Sec. III B 2 (see details in Sec. SIII of the Supplemental material [42]). This is a direct consequence of including more DFT information in the fit, while keeping our model very simple. For example, our numerical fit includes all the information about the super-tetragonal state P[001], which features significantly larger polarization and strains compared to other polymorphs. This allows us to predict more accurately the polarization of this polymorph; however, it leads to worse predictions for some critical properties (e.g., the ground-state energy) compared to the analytically derived model in which information on the P[001] state was barely used. We thus conclude that, while the numerical approach might work well for more complete, higher-order potentials (for example, such as the one introduced in Ref. [45]), it seems less suitable for computing the parameters of our low-order model. Therefore, in the following, we are going to discuss only the results obtained using the analytical approach.

## IV. RESULTS

### A. BiFeO<sub>3</sub>

In this section, we analyze how accurately the potential introduced in Sec. III A predicts the properties of BiFeO<sub>3</sub> polymorphs. We begin by computing the coefficients of the potential following the analytical approach described in Sec. III B 2. The resulting values are presented in Table III. Next, we use the computed potential to calculate the

TABLE III. Coefficients of our Landau-like potentials calculated for BiFeO<sub>3</sub> (BFO) and La<sub>0.25</sub>Fe<sub>0.75</sub>FeO<sub>3</sub> (LBFO) using the analytical approach introduced in Sec. III B 2. We give energies per five-atom perovskite unit cell.

	BFO	LBFO	Units
$A_P$	-1.747	-1.674	$\times 10^{-19}, \text{J m}^4 \text{C}^{-2}$
$B_P$	1.070	1.286	$\times 10^{-19}, \text{J m}^8 \text{C}^{-4}$
$C_P$	-7.486	-6.212	$\times 10^{-20}, \text{J m}^8 \text{C}^{-4}$
$A_R$	-8.555	-7.560	$\times 10^{-22}, \text{J deg}^{-2}$
$B_R$	2.169	1.962	$\times 10^{-24}, \text{J deg}^{-4}$
$C_R$	-1.240	-0.848	$\times 10^{-24}, \text{J deg}^{-4}$
$C_{11}$	1.833	1.754	$\times 10^{-17}, \text{J}$
$C_{12}$	7.301	11.280	$\times 10^{-18}, \text{J}$
$C_{44}$	4.600	4.262	$\times 10^{-18}, \text{J}$
$B_{PR}$	1.121	1.183	$\times 10^{-21}, \text{J m}^4 \text{C}^{-2} \text{deg}^{-2}$
$C_{PR}$	-3.437	-3.319	$\times 10^{-22}, \text{J m}^4 \text{C}^{-2} \text{deg}^{-2}$
$C'_{PR}$	-2.245	-2.219	$\times 10^{-21}, \text{J m}^4 \text{C}^{-2} \text{deg}^{-2}$
$\gamma_{P111}$	-9.444	-7.866	$\times 10^{-19}, \text{J m}^4 \text{C}^{-2}$
$\gamma_{P122}$	-1.557	-4.898	$\times 10^{-19}, \text{J m}^4 \text{C}^{-2}$
$\gamma_{P423}$	-3.232	-3.359	$\times 10^{-19}, \text{J m}^4 \text{C}^{-2}$
$\gamma_{R111}$	-1.178	0.482	$\times 10^{-21}, \text{J deg}^{-2}$
$\gamma_{R122}$	1.158	-10.026	$\times 10^{-22}, \text{J deg}^{-2}$
$\gamma_{R423}$	1.155	1.022	$\times 10^{-21}, \text{J deg}^{-2}$

equilibrium properties ( $\mathbf{P}_s$ ,  $\mathbf{R}_s$ ,  $\eta_s$ , and  $E_s$ ) of the polymorphs 1c to 6c and 1 to 6. Since in these polymorphs the form of  $\mathbf{P}_s$  is either  $(0, 0, P_s)$  or  $(P_s, P_s, P_s)$  (the same holds for  $\mathbf{R}_s$ ), in the following we will discuss single components of  $\mathbf{P}_s$  and  $\mathbf{R}_s$  ( $P_s$  and  $R_s$ , respectively). We plot the values of  $P_s$ ,  $R_s$ , and  $E_s$  predicted using our potential versus their DFT counterparts as shown in Fig. 3 (all these values, as well as the components of  $\eta_s$  are also presented in Table S1 of the Supplemental Material [42]). We note that, if the model prediction and DFT value match exactly, the corresponding point lays on the black dashed line.

First, we discuss the BiFeO<sub>3</sub> polymorphs with the fixed cubic cell (no strain relaxation). From Figs. 3(a) and 3(b) one can see that, for these polymorphs, our model predicts  $P_s$  and  $R_s$  in nearly perfect agreement with DFT. As shown in Fig. 3(c), it also accurately reproduces their energies and, therefore, their relative stability. Indeed, among the structures having only polar distortion (P[001]c and P[111]c), the one with  $\mathbf{P} \parallel [111]$  is lower in energy according to both model and DFT. The same holds for the structures having only FeO<sub>6</sub> octahedral rotations (R[111]c is lower in energy than R[001]c). Overall, the lowest energy structure is P[111]+R[111]c, in which both distortions coexist and oriented along/about [111]. Here, one should keep in mind that DFT information about these polymorphs is explicitly used to compute the model parameters (see Table II), hence the agreement is not surprising. Nevertheless, the potential does provide accurate predictions for quantities that are not considered in its derivation (e.g.,  $P$  of P[001]c,  $R$  of R[001]c, and  $E_s$  of P[001]+R[001]c and P[111]+R[111]c).

Next, we consider the BiFeO<sub>3</sub> polymorphs with allowed strain relaxation [Figs. 3(d)–3(f)]. In this case, our potential also provides accurate predictions for all considered quantities for the most of the considered polymorphs; in particular, it yields the correct ground state of BiFeO<sub>3</sub> (P[111]+R[111]). There is only one polymorph for which the model is less accurate, namely, P[001]. In this case, the DFT optimized structure has a large distortion along the  $z$  axis (the  $c/a$  ratio is approximately 1.27), accompanied by a large  $P_z$ ; this is usually called a supertetragonal phase [46,47]. This behavior is not well captured by our potential, as it underestimates the polarization and strains components compared to the DFT values ( $P_z = 1.039$  versus  $1.624 \text{ C/m}^2$ ;  $\eta_{xx} = -0.012$  versus  $-0.044$ ;  $\eta_{zz} = 0.065$  versus  $0.216$ ). This issue is also reflected in the energy predicted for this phase. From the DFT results, one can see that, among the polymorphs with only polar distortion, the strain relaxation stabilizes the supertetragonal phase over the rhombohedral one (P[001] is lower than P[111]

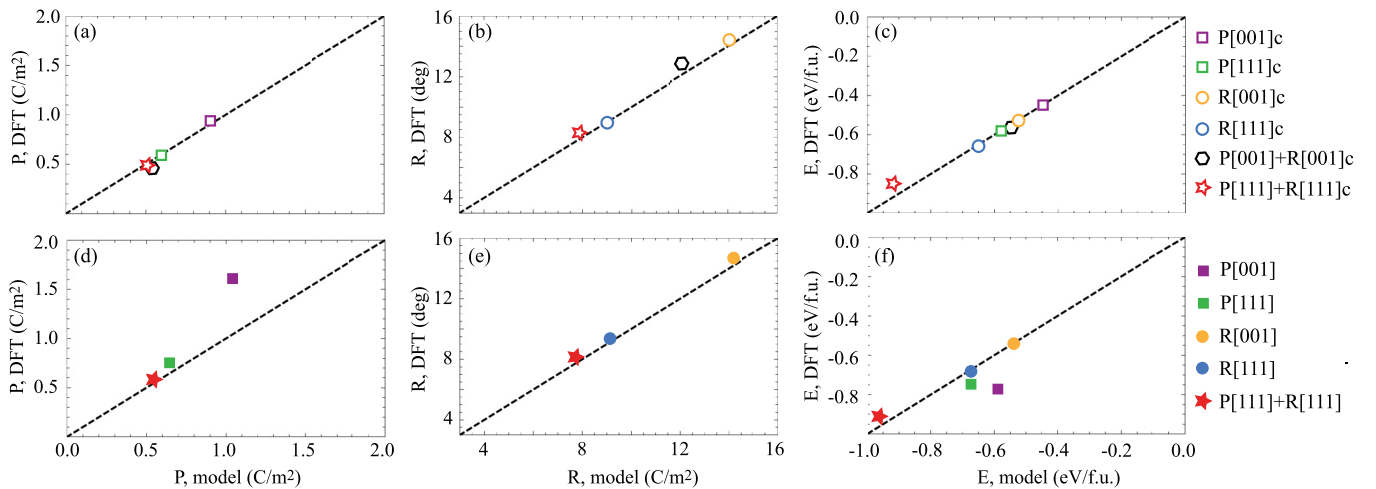


FIG. 3. Structural properties and energies of BiFeO<sub>3</sub> polymorphs predicted using the Landau-like potential and plotted versus their corresponding DFT values. The top row shows the results obtained for the polymorphs with fixed cubic supercell (no strain), while the bottom row shows the properties of the polymorphs with fully relaxed cells. Panels (a) and (d) show the electric polarization  $P$ , (b) and (e) the FeO<sub>6</sub> octahedral rotations  $R$ , (c) and (f) the energies  $E$ . The polymorph P[001]+R[001] is not shown in panels (d)–(f), since its fully relaxed structure has very small FeO<sub>6</sub> octahedral rotations ( $R = 0.066^\circ$ ) and our model predicts it to be zero, therefore reducing to the state P[001].

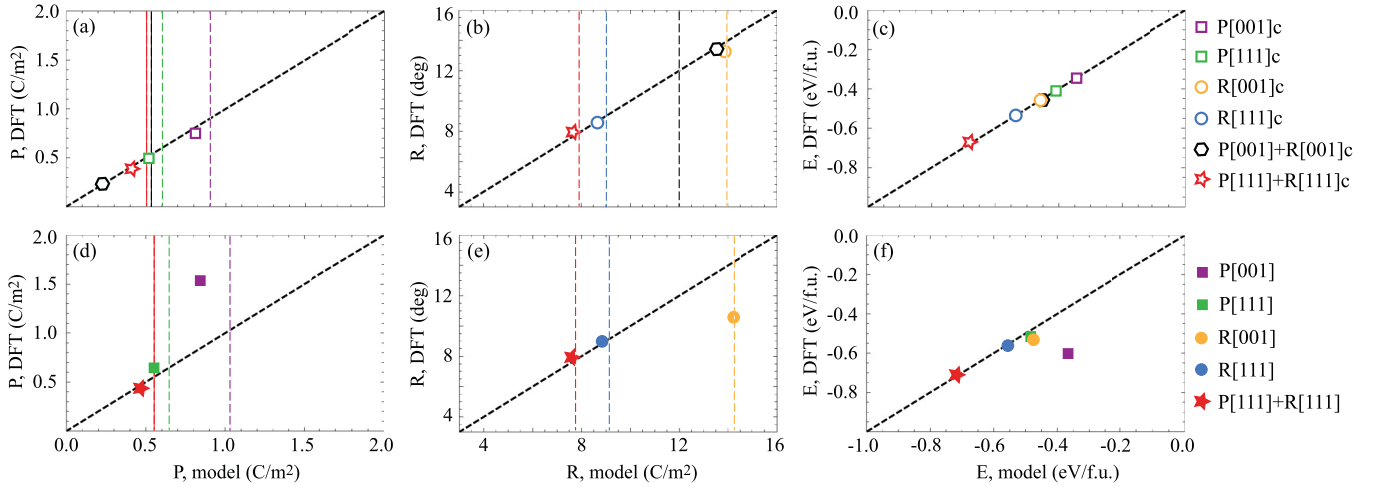


FIG. 4. Structural properties and energies of  $\text{La}_{0.25}\text{Bi}_{0.75}\text{FeO}_3$  polymorphs predicted using the Landau-like potential and plotted versus their corresponding DFT values. The top row shows the results obtained for the polymorphs with fixed cubic supercell (no strain), while the bottom row shows the properties of the polymorphs with fully relaxed cells. Panels (a) and (d) show the electric polarization  $P$ , (b) and (e) the  $\text{FeO}_6$  octahedral rotations  $R$ , (c) and (f) the energies  $E$ . The polymorph  $\text{P}[001]+\text{R}[001]$  is not shown in panels (d)–(f), since its fully relaxed structure has very small  $\text{FeO}_6$  octahedral rotations ( $R = 0.006^\circ$ ) and our model predicts it to be zero, therefore reducing to the state  $\text{P}[001]$ . The vertical dashed lines in panels (a), (b), (d), and (e) indicate the corresponding quantities for pure  $\text{BiFeO}_3$ .

by  $0.023 \text{ eV/f.u.}$ ). Our model does predict the energy lowering of the  $\text{P}[001]$  state due to the strain relaxation (the negative  $\gamma_{\text{P}111}$  coupling results in large  $P_z$  and  $\eta_{zz}$ ). However, since it underestimates  $P_z$  and  $\eta_{zz}$ , this energy reduction is not enough to stabilize  $\text{P}[001]$  over  $\text{P}[111]$ . Note that these deficiencies were to be expected, as we decided to use a minimal amount of DFT information on the supertetragonal phase when deriving the parameters of our model (see Table II) because this state is not relevant for our ultimate purpose of studying polarization switching in the rhombohedral phase of  $\text{BiFeO}_3$ . Moreover, we checked that, if we try to capture the supertetragonal  $c/a$ , this makes it difficult to obtain a correct prediction for the ground state, as the  $\text{P}[001]$  state tends to become dominant.

### B. $\text{La}_{0.25}\text{Bi}_{0.75}\text{FeO}_3$

Now we discuss the case of  $\text{La}_{0.25}\text{Bi}_{0.75}\text{FeO}_3$ . We first compute the parameters of the potential using the analytical expressions in Sec. III B 2. The resulting values are presented in Table III. Next, we compare the model predictions and DFT values for our considered polymorphs in Fig. 4 (these results are also summarized in Table S2 of the Supplemental Material [42], together with the corresponding strains).

Let us first consider the polymorphs with fixed cubic cell [Figs. 4(a)–4(c)]. Our potential provides very accurate predictions for polarizations and tilts, similarly to the case of pure  $\text{BiFeO}_3$ . The energy and relative stability of these polymorphs is also well captured by the model. Indeed, for polar-only structures, both the model and DFT predict the rhombohedral  $\text{P}[111]\text{c}$  state to be lower in energy than the tetragonal  $\text{P}[001]\text{c}$  phase. The same holds for the polymorphs having only  $\text{FeO}_6$  rotations:  $\text{R}[111]\text{c}$  is lower in energy than  $\text{R}[001]\text{c}$ . Note that the energy difference between the structures with tetragonal and rhombohedral phases are reduced compared to the case of pure  $\text{BiFeO}_3$ . The lowest-energy phase is  $\text{P}[111]+\text{R}[111]\text{c}$ , where polarization and tilts coexist.

For the polymorphs in which shape and volume of the cell are allowed to relax, we observe the following. First, the model predicts accurate values of the polarization in all cases except for  $\text{P}[001]$ . Indeed, for the supertetragonal state, the predicted  $P_x$  and  $\eta_{zz}$  are underestimated relative to the DFT values. This issue is also reflected in the energy of the polymorph: our potential predicts  $\text{P}[001]$  to be the highest-energy state, while DFT shows that this phase is the second-lowest in energy, right above the  $\text{P}[111]+\text{R}[111]$  ground state. Additionally, we find that the tilts are accurately predicted by our model for all polymorphs except  $\text{R}[001]$ ; in that case, the tilt amplitude and the strains are exaggerated compared to the DFT values. Note that, as in the case for pure  $\text{BiFeO}_3$ , these deficiencies are the result of the limited amount of DFT information on states  $\text{P}[001]$  and  $\text{R}[001]$  used to derive the parameters of our model.

### C. Intermediate compositions

In this section, we demonstrate how our potentials can be used to study  $\text{La}_{1-x}\text{Bi}_x\text{FeO}_3$  with intermediate La content,  $0 < x < 0.25$ .

Let us assume that the La doping acts on the properties of  $\text{BiFeO}_3$  as a perturbation. We can write a general expression for any quantity of interest (which we denote as  $f$ ) in the following form:

$$f = f_0 + x f_1 + x^2 f_2 + \dots, \quad (35)$$

where  $f_0$  is the unperturbed value,  $x$  is the La concentration, and  $f_1, f_2, \dots$  are corrections of increasing order. Let us imagine we can truncate the perturbation series and keep only the first two terms such that

$$f \approx f_0 + x f_1. \quad (36)$$

This approximation complies with the empirically determined Vegard's law, according to which an approximately linear



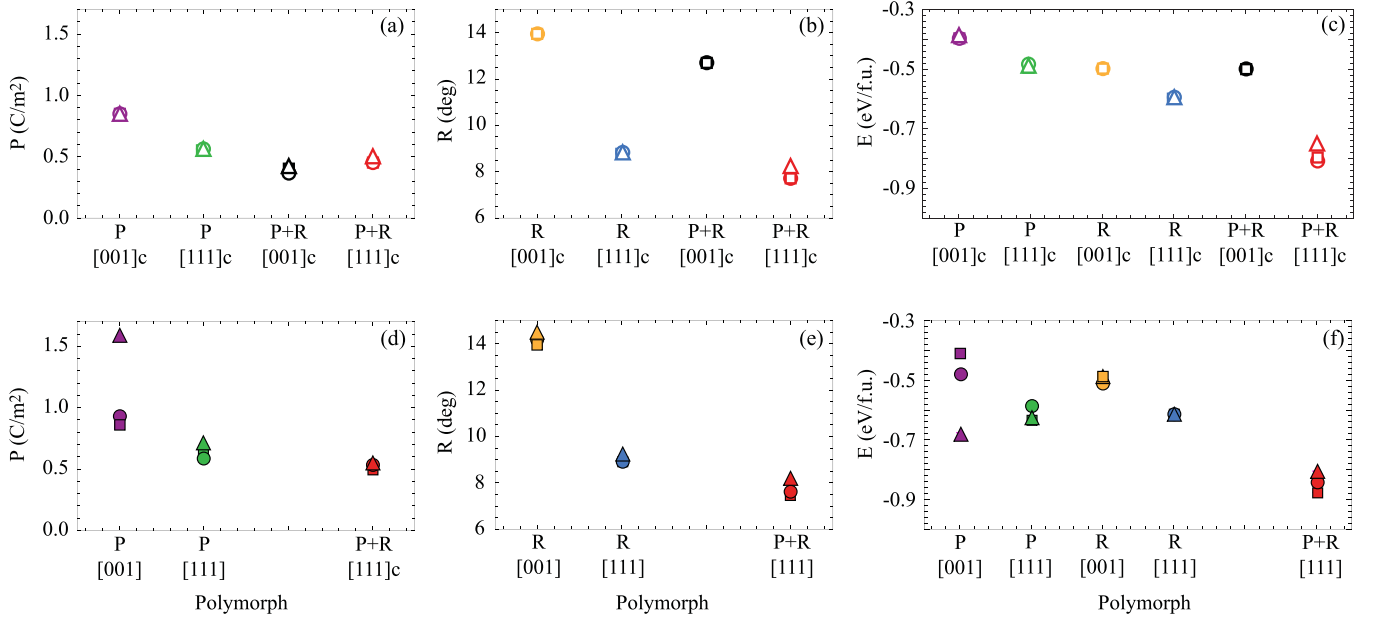


FIG. 5. Structural properties and energies of  $\text{La}_{0.125}\text{Bi}_{0.875}\text{FeO}_3$  polymorphs. Squares show the model predictions for  $P$ ,  $R$ , and  $E$  obtained using the interpolated potential's coefficients; circles: the values obtained by direct interpolation of the corresponding results between pure  $\text{BiFeO}_3$  and  $\text{La}_{0.25}\text{Bi}_{0.75}\text{FeO}_3$ ; triangles: DFT values. The top row shows the results for fixed cubic cell (no strain); bottom row: results after a full strain relaxation. Panels (a) and (d) show the electric polarization  $P$ , (b) and (e) the  $\text{FeO}_6$  octahedral rotations  $R$ , (c) and (f) the energies  $E$ . A missing DFT data point in the plot means that the structure of the corresponding polymorph developed non-negligible additional distortions during the DFT optimization, as described in Sec. III B 1.

relation exists between properties of an alloy and the concentrations of the constituent elements at a constant temperature [48].

Here we focus on the case of  $\text{La}_{0.125}\text{Bi}_{0.875}\text{FeO}_3$  and check whether the properties of the polymorphs from the data set can indeed be predicted by linear interpolation between  $\text{BiFeO}_3$  and  $\text{La}_{0.25}\text{Bi}_{0.75}\text{FeO}_3$ .

We consider two types of interpolation. First, we construct a model for  $x = 0.125$  with coefficients obtained from interpolation of the corresponding values for the  $x = 0$  and  $x = 0.25$  cases. Using this model, we can easily predict the properties ( $P_s$ ,  $R_s$ , and  $E_s$ ) of all the polymorphs in the data set. Second, we derive the very same properties by direct interpolation of the values obtained at  $x = 0$  and  $x = 0.25$ . In Fig. 5, we compare the quantities thus obtained, and also include the corresponding DFT values for the polymorphs for which the information is available (see figure caption and Table S4 of the Supplemental Material [42]). We find that both interpolation approaches yield very similar predictions. Further, the agreement with DFT is good except for the supertetragonal P[001] phase, where our predictions suffer from the issues discussed above. Hence, we conclude that our models give us a way to treat compounds with intermediate compositions.

## V. DISCUSSION

Let us now discuss the physical insights that our models provide.

### A. P-R coupling

As is well-known from both experiments and computations, and correctly captured by our models, the ground state

of  $\text{BiFeO}_3$  has rhombohedral symmetry with  $\mathbf{P} \parallel [111]$  and  $\mathbf{R} \parallel [111]$ . It is interesting to note, though, that the DFT energy of the polar-only  $\text{BiFeO}_3$  polymorph P[001] is lower than that of P[111]. By contrast, among the polymorphs having only  $\text{FeO}_6$  octahedral tilts, R[111] is the lowest-energy structure. These observations yield one important conclusion: that the rhombohedral symmetry of the  $\text{BiFeO}_3$ 's ground state critically depends on the presence of the octahedral tilts, as in their absence the material would be tetragonal.

To understand how the rhombohedral ground state of  $\text{BiFeO}_3$  comes about, we consider the  $F(\mathbf{P}, \mathbf{R})$  part of our potential [Eq. (5)] describing the coupling between polarization and octahedral rotations. The second term in Eq. (5), with  $C_{PR} < 0$  (see Table III), favors states where  $\mathbf{P}$  and  $\mathbf{R}$  are along/about any  $\langle 111 \rangle$  direction, as, for example,  $\mathbf{P} \parallel [111]$  and  $\mathbf{R} \parallel [\bar{1}\bar{1}\bar{1}]$ . In turn, the third term, with  $C'_{PR} < 0$ , favors phases where the  $\text{FeO}_6$  tilts are about the axis defined by the polarization. Overall, these couplings lead  $\mathbf{P}$  and  $\mathbf{R}$  to appear together and aligned along/about the same  $\langle 111 \rangle$  direction. Thus, these are the interactions driving the stabilization of the ground-state phase of  $\text{BiFeO}_3$ , rhombohedral, and with coexisting polarization and tilts.

Does this mean, however, that  $\mathbf{P}$  and  $\mathbf{R}$  cooperate in  $\text{BiFeO}_3$ ? We address this question by considering the energy diagram presented in Fig. 6. Here we show the energies of the P[111]c, R[111]c, and P[111]+R[111]c polymorphs as given by our model ( $E_{2c}$ ,  $E_{4c}$ , and  $E_{6c}$ , respectively, see Table IV). We also show the energy of a nonexistent, virtual state in which  $\mathbf{P} \parallel [111]$  coexists with  $\mathbf{R} \parallel [111]$  but where these order parameters are not coupled. The energy of this virtual state corresponds to the most stable rhombohedral polymorph predicted by our model when all the  $\mathbf{P}$ - $\mathbf{R}$

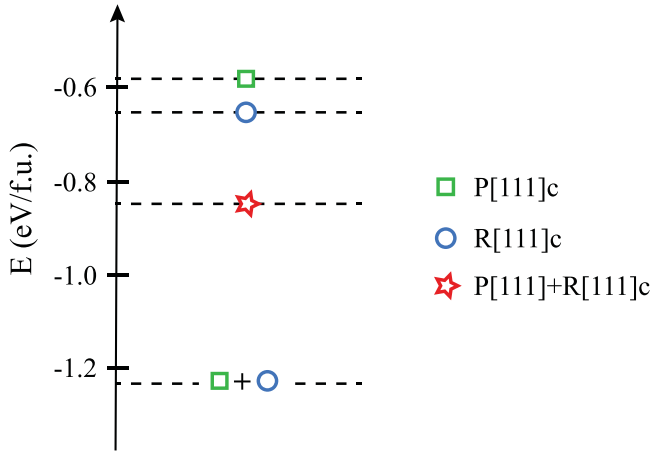


FIG. 6. Illustration of the effect of the coupling between polarization  $\mathbf{P}$  and  $\text{FeO}_6$  octahedral tilts  $\mathbf{R}$  on the energetics of  $\text{BiFeO}_3$  polymorphs. Model energies of  $\text{BiFeO}_3$  polymorphs P[111]c, R[111]c, and P[111]+R[111]c with fixed cubic supercell are shown, together with the energy of the nonexistent, virtual state in which  $\mathbf{P} \parallel [111]$  and  $\mathbf{R} \parallel [111]$  coexist but are not coupled (indicated as square+circle in the figure, see more details in the text). Since the energy of this virtual noninteracting state is lower than that of the actual state P[111]+R[111]c, one can conclude that  $\mathbf{P}$  and  $\mathbf{R}$  compete in  $\text{BiFeO}_3$ .

couplings are artificially set to zero. Clearly, the P[111]+R[111]c polymorph is higher in energy than the noninteracting virtual state and their energy difference arises from the coupling between  $\mathbf{P}$  and  $\mathbf{R}$  in P[111]+R[111]c structure. To understand this, we again consider the term  $F(\mathbf{P}, \mathbf{R})$  [Eq. (5)] with the corresponding coefficients  $B_{PR}$ ,  $C_{PR}$ , and  $C'_{PR}$  presented in Table III for  $\text{BiFeO}_3$ . For the polymorph P[111]+R[111]c, we have  $P_x = P_y = P_z = P_{6c}$  and  $R_x = R_y = R_z = R_{6c}$ ; therefore,  $F_{6c}(\mathbf{P}, \mathbf{R}) = 3(3B_{PR} + C_{PR} + C'_{PR})P_{6c}^2 R_{6c}^2$  for this state. In this expression,  $3B_{PR} > 0$  dominates over  $C_{PR} + C'_{PR} < 0$  and

TABLE IV. Energies  $E_s$  of  $\text{BiFeO}_3$  polymorphs calculated using DFT and predicted by the Landau-like potential introduced in this paper (the coefficients of the potential are obtained using the analytical approach described in Sec. III B 2). Energy values are relative to the energy of the reference cubic phase and given in eV per five-atom unit cell.

	Polymorph	$E_s$ (DFT)	$E_s$ (Model)
1c	P[001]c	-0.445	-0.445
2c	P[111]c	-0.580	-0.580
3c	R[001]c	-0.527	-0.527
4c	R[111]c	-0.651	-0.650
5c	P[001]+R[001]c	-0.556	-0.546
6c	P[111]+R[111]c	-0.853	-0.919
1	P[001]	-0.764	-0.589
2	P[111]	-0.741	-0.677
3	R[001]	-0.536	-0.540
4	R[111]	-0.679	-0.671
5	P[001]+R[001]	-0.764	-0.593
6	P[111]+R[111]	-0.909	-0.967

leads to a ground-state energy that is higher than that of the virtual noninteracting state.

Thus, we find that, overall, the  $\mathbf{P}$  and  $\mathbf{R}$  order parameters compete in  $\text{BiFeO}_3$  ( $B_{PR} > 0$  dominates). Nevertheless, the polar and tilt instabilities are so strong that this repulsive interaction is not enough to prevent them from occurring simultaneously. Further, the  $\mathbf{P}$ - $\mathbf{R}$  competition is minimized when the order parameters are oriented along/about the same  $\langle 111 \rangle$  axis ( $C_{PR}, C'_{PR} < 0$ ), which yields the rhombohedral ground state phase of  $\text{BiFeO}_3$ .

## B. Effects of La doping

Let us first consider how La doping affects the electric polarization. From Figs. 4(a) and 4(d), one can see that, for all considered polar polymorphs in the data set, a 25% La doping leads to reduction of  $P$ . Indeed, for the polymorphs with fixed cubic cell [Fig. 4(a)], we obtain a reduction of  $P$  by 11 – 19% for P[001]c, P[111]c, and P[111]+R[111]c, and an even larger reduction for P[001]+R[001]c ( $\approx 59\%$ ). When we allow the cell to relax [Fig. 4(d)], the obtained  $P$  reduction is in the range of 5 – 20%.

Next, let us turn to the effect of La doping on the  $\text{FeO}_6$  octahedral tilts. As one can see from Figs. 4(b) and 4(e), the presence of 25% La has a relatively small effect (reduction) in the amplitude of tilts. More precisely, we find that the R[001]c, R[111]c, and P[111]+R[111]c polymorphs with fixed cubic cell present 1 – 4% smaller  $R$  compared to pure  $\text{BiFeO}_3$ . The exception is the P[001]+R[001]c state, where La doping leads to an increase in  $R$  by 12%. Finally, when we allow the cell to relax, we find a 0.06 – 4% reduction of  $R$  in all considered polymorphs.

Our models allow us to rationalize the most important results described above. Let us start by noting that the  $\mathbf{P}$ - $\mathbf{R}$  couplings [ $B_{PR}$ ,  $C_{PR}$ , and  $C'_{PR}$  in  $F(\mathbf{P}, \mathbf{R})$ ] are not significantly affected by the doping. Hence, they do not play a significant role to explain the La-induced effects.

Indeed, the effects of La doping on the polarization are essentially captured by the changes in the  $F(\mathbf{P})$  term of the potential [Eq. (2)]. As shown in Table III, we find that  $A_P$  (quadratic coupling) is reduced in magnitude upon doping, indicating a weaker ferroelectric instability of the cubic phase. Additionally, both  $B_P$  and  $C_P$  increase and the relevant combination,  $3B_P + C_P > 0$ , becomes larger; hence, the quartic couplings have a stronger effect on the energy landscape compared to pure  $\text{BiFeO}_3$ . All these changes cooperate to yield shallower ferroelectric energy wells associated to  $F(\mathbf{P})$  for La-doped  $\text{BiFeO}_3$ , with smaller equilibrium polarization and lower energy barrier between states of opposite  $\mathbf{P}$ . Note that this is consistent with previous studies on the effect of La doping on the switching characteristics of  $\text{BiFeO}_3$  [24,28].

With regard to the tilt energy given by  $F(\mathbf{R})$ , Table III shows that the presence of La weakens the cubic-phase instability ( $A_R$  becomes less negative); by contrast, the quartic term ( $3B_R + C_R > 0$ ) gets reduced upon doping, thus favoring larger tilts. These changes oppose each other, and result in the generally observed moderate reduction in the amplitude of the  $\text{FeO}_6$  rotations.

Finally, as shown in Fig. 4, the P[001]+R[001]c case is peculiar, as it presents the largest reduction in  $P$  (about

59%) and is the only one displaying an increase of  $R$  (about 12%). We can rationalize this result by noting that, for this state, the quartic part of the energy in  $F(\mathbf{P})$  [respectively,  $F(\mathbf{R})$ ] is controlled by the  $B_P$  (respectively,  $B_R$ ) coupling alone. Upon doping,  $B_P$  grows ( $B_R$  decreases), which favors smaller polarizations (larger tilts). Further, because of the strong competition between polarization and tilts in tetragonal states ( $B_{PR} > 0$ ;  $C_{PR}$  and  $C'_{PR}$  do not contribute), the changes get particularly large in the case of P[001]+R[001]c. Note also a subtle difference between P[001]+R[001]c and P[111]+R[111]c. In the latter case, the relevant quartic parameter for the tilts is  $3B_R + C_R$ , and the La-induced decrease in  $B_R$  is partly compensated by the increase in  $C_R$ ; as a result, the tilts do not grow at all (recall  $A_R < 0$  grows upon doping) and the decrease of the polarization is relatively small.

Note that all these observations are consistent with what we know about the atomistic origin of the polar and tilt instabilities in BiFeO<sub>3</sub>. The former rely on the presence of stereochemically active 6s lone pairs in the Bi<sup>3+</sup> cations; hence, their partial substitution by lone-pair-free La cations naturally leads to smaller polarizations. The latter are mainly controlled by the ionic radius of the Bi<sup>3+</sup> cation; since La<sup>3+</sup> is similar in size, the doping leaves  $R$  largely unaffected.

## VI. CONCLUSIONS

In summary, we have introduced the simplest, lowest-order Landau-like potential for BiFeO<sub>3</sub> and related compounds, as well as methods that allow us to compute the potential parameters from DFT. More precisely, we have derived analytical expressions for all the model coefficients as func-

tions of the energies and structural features (polarization, FeO<sub>6</sub> octahedral tilts, and strains) of a small set of relevant polymorphs. We have applied the proposed approach to BiFeO<sub>3</sub> and La<sub>0.25</sub>Bi<sub>0.75</sub>FeO<sub>3</sub>, showing its overall accuracy in reproducing the DFT data. We have also showed that our models can be used—by interpolation—to predict the properties of compounds with intermediate dopant concentrations. We note that the introduced potential, as well as the analytical scheme to obtain its coefficients from DFT, can be readily applied to study the properties of other perovskite oxides characterized by the same order parameters (polarization, antiphase oxygen-octahedral tilts, and strains). This includes ferroelectrics where the tilts are not important (e.g., BaTiO<sub>3</sub> or PbTiO<sub>3</sub>), antiferrodistortive nonpolar perovskites (e.g., LaAlO<sub>3</sub>), or compounds where both distortions play a relevant role (e.g., SrTiO<sub>3</sub>; potentially, 5d perovskites like LiOsO<sub>3</sub> and NaOsO<sub>3</sub> [49,50]), as well as their corresponding solid solutions. In principle, an extension of our scheme to compounds where other order parameters are relevant (e.g., in-phase tilts in orthorhombic perovskites like CaTiO<sub>3</sub> [51]) should be straightforward.

## ACKNOWLEDGMENTS

We thank John M. Mangeri for the fruitful discussions. Work funded by the the Semiconductor Research Corporation and Intel via Contract No. 2018-IN-2865. We also acknowledge the support of the Luxembourg National Research Fund through Grant No. FNR/C18/MS/12705883/REFOX/Gonzalez.

- 
- [1] N. A. Spaldin and M. Fiebig, *Science* **309**, 391 (2005).
  - [2] W. Eerenstein, N. D. Mathur, and J. F. Scott, *Nature (London)* **442**, 759 (2006).
  - [3] G. Catalan and J. F. Scott, *Adv. Mater.* **21**, 2463 (2009).
  - [4] J. Moreau, C. Michel, R. Gerson, and W. James, *J. Phys. Chem. Solids* **32**, 1315 (1971).
  - [5] R. T. Smith, G. D. Achenbach, R. Gerson, and W. J. James, *J. Appl. Phys.* **39**, 70 (1968).
  - [6] C. Michel, J.-M. Moreau, G. D. Achenbach, R. Gerson, and W. James, *Solid State Commun.* **7**, 701 (1969).
  - [7] F. Kubel and H. Schmid, *Acta Crystallogr. Sect. B* **46**, 698 (1990).
  - [8] R. Seshadri and N. A. Hill, *Chem. Mater.* **13**, 2892 (2001).
  - [9] D. Lebeugle, D. Colson, A. Forget, and M. Viret, *Appl. Phys. Lett.* **91**, 022907 (2007).
  - [10] J. Wang, J. B. Neaton, H. Zheng, V. Nagarajan, S. B. Ogale, B. Liu, D. Viehland, V. Vaithyanathan, D. G. Schlom, U. V. Waghmare *et al.*, *Science* **299**, 1719 (2003).
  - [11] A. M. Glazer, *Acta Crystallogr. Sect. B* **28**, 3384 (1972).
  - [12] C. Ederer and N. A. Spaldin, *Phys. Rev. B* **71**, 060401(R) (2005).
  - [13] O. Diéguez, O. E. González-Vázquez, J. C. Wojdeł, and J. Íñiguez, *Phys. Rev. B* **83**, 094105 (2011).
  - [14] V. Bhide and M. Multani, *Solid State Commun.* **3**, 271 (1965).
  - [15] I. Dzyaloshinsky, *J. Phys. Chem. Solids* **4**, 241 (1958).
  - [16] T. Moriya, *Phys. Rev.* **120**, 91 (1960).
  - [17] I. Sosnowska, T. P. Neumaier, and E. Steichele, *J. Phys. C* **15**, 4835 (1982).
  - [18] I. Sosnowska, W. Schäfer, W. Kockelmann, K. H. Andersen, and I. O. Troyanchuk, *Appl. Phys. A* **74**, s1040 (2002).
  - [19] F. Bai, J. Wang, M. Wuttig, J. Li, N. Wang, A. P. Pyatakov, A. K. Zvezdin, L. E. Cross, and D. Viehland, *Appl. Phys. Lett.* **86**, 032511 (2005).
  - [20] H. Béa, M. Bibes, S. Petit, J. Kreisel, and A. Barthélémy, *Philos. Mag. Lett.* **87**, 165 (2007).
  - [21] D. Sando, A. Agbelele, D. Rahmedov, J. Liu, P. Rovillain, C. Toulouse, I. C. Infante, A. P. Pyatakov, S. Fusil, E. Jacquet *et al.*, *Nat. Mater.* **12**, 641 (2013).
  - [22] J. T. Heron, J. L. Bosse, Q. He, Y. Gao, M. Trassin, L. Ye, J. D. Clarkson, C. Wang, J. Liu, S. Salahuddin *et al.*, *Nature (London)* **516**, 370 (2014).
  - [23] S. Manipatruni, D. E. Nikonov, and I. A. Young, *Nat. Phys.* **14**, 338 (2018).
  - [24] B. Prasad, Y.-L. Huang, R. V. Chopdekar, Z. Chen, J. Steffes, S. Das, Q. Li, M. Yang, C.-C. Lin, T. Gosavi *et al.*, *Adv. Mater.* **32**, 2001943 (2020).
  - [25] Y. H. Chu, Q. Zhan, C.-H. Yang, M. P. Cruz, L. W. Martin, T. Zhao, P. Yu, R. Ramesh, P. T. Joseph, I. N. Lin *et al.*, *Appl. Phys. Lett.* **92**, 102909 (2008).
  - [26] O. E. González-Vázquez, J. C. Wojdeł, O. Diéguez, and J. Íñiguez, *Phys. Rev. B* **85**, 064119 (2012).

- [27] L. Zhang, Y.-L. Huang, G. Velarde, A. Ghosh, S. Pandya, D. Garcia, R. Ramesh, and L. W. Martin, *APL Mater.* **7**, 111111 (2019).
- [28] E. Parsonnet, Y.-L. Huang, T. Gosavi, A. Qualls, D. Nikonov, C.-C. Lin, I. Young, J. Bokor, L. W. Martin, and R. Ramesh, *Phys. Rev. Lett.* **125**, 067601 (2020).
- [29] L. D. Landau, *Zh. Eksp. Teor. Fiz.* **7**, 19 (1937).
- [30] L. D. Landau, *Zh. Eksp. Teor. Fiz.* **7**, 627 (1937).
- [31] A. Devonshire, *London, Edinburgh, Dublin Philos. Mag. J. Sci.* **40**, 1040 (1949).
- [32] A. Devonshire, *London, Edinburgh, Dublin Philos. Mag. J. Sci.* **42**, 1065 (1951).
- [33] A. Umantsev, *Field Theoretic Method in Phase Transformations* (Springer, New York, 2012).
- [34] K. Rabe, C. H. Ahn, and J.-M. Triscone, *Physics of Ferroelectrics. A Modern Perspective* (Springer, Berlin, 2007).
- [35] P. Hohenberg and W. Kohn, *Phys. Rev.* **136**, B864 (1964).
- [36] W. Kohn and L. J. Sham, *Phys. Rev.* **140**, A1133 (1965).
- [37] G. Kresse and J. Furthmüller, *Phys. Rev. B* **54**, 11169 (1996).
- [38] J. P. Perdew, A. Ruzsinszky, G. I. Csonka, O. A. Vydrov, G. E. Scuseria, L. A. Constantin, X. Zhou, and K. Burke, *Phys. Rev. Lett.* **100**, 136406 (2008).
- [39] S. L. Dudarev, G. A. Botton, S. Y. Savrasov, C. J. Humphreys, and A. P. Sutton, *Phys. Rev. B* **57**, 1505 (1998).
- [40] P. E. Blöchl, *Phys. Rev. B* **50**, 17953 (1994).
- [41] Y. Le Page and P. Saxe, *Phys. Rev. B* **65**, 104104 (2002).
- [42] See Supplemental Material at <http://link.aps.org/supplemental/10.1103/PhysRevB.106.165122> for tables with first-principles and Landau-like model predictions for the structural properties and the energies of BiFeO<sub>3</sub> and La-doped BiFeO<sub>3</sub> polymorphs.
- [43] L. Bellaïche and D. Vanderbilt, *Phys. Rev. B* **61**, 7877 (2000).
- [44] J. Íñiguez, D. Vanderbilt, and L. Bellaïche, *Phys. Rev. B* **67**, 224107 (2003).
- [45] P. Marton, A. Klíř, M. Pařciak, and J. Hlinka, *Phys. Rev. B* **96**, 174110 (2017).
- [46] H. Béa, B. Dupé, S. Fusil, R. Mattana, E. Jacquet, B. Warot-Fonrose, F. Wilhelm, A. Rogalev, S. Petit, V. Cros *et al.*, *Phys. Rev. Lett.* **102**, 217603 (2009).
- [47] R. J. Zeches, M. D. Rossell, J. X. Zhang, A. J. Hatt, Q. He, C.-H. Yang, A. Kumar, C. H. Wang, A. Melville, C. Adamo *et al.*, *Science* **326**, 977 (2009).
- [48] A. R. Denton and N. W. Ashcroft, *Phys. Rev. A* **43**, 3161 (1991).
- [49] P. Liu, J. He, B. Kim, S. Khmelevskyi, A. Toschi, G. Kresse, and C. Franchini, *Phys. Rev. Mater.* **4**, 045001 (2020).
- [50] R. Sereika, P. Liu, B. Kim, S. Kim, J. Zhang, B. Chen, K. Yamaura, C. Park, C. Franchini, Y. Ding *et al.*, *npj Quantum Mater.* **5**, 66 (2020).
- [51] P. Chen, M. N. Grisolia, H. J. Zhao, O. E. González-Vázquez, L. Bellaïche, M. Bibes, B.-G. Liu, and J. Íñiguez, *Phys. Rev. B* **97**, 024113 (2018).